Published online 18 October 2011 *Nucleic Acids Research, 2012, Vol. 40, No. 3* ***1345–1355***
doi:10.1093/nar/gkr833

Unraveling the structural complexity in a single-stranded RNA tail: implications for efficient ligand binding in the prequeuosine riboswitch

Catherine D. Eichhorn[1], Jun Feng[2,3], Krishna C. Suddala[2,3], Nils G. Walter[2], Charles L. Brooks III[1,2,3,4,*] and Hashim M. Al-Hashimi[1,2,3,*]

[1]Chemical Biology Doctoral Program, [2]Department of Chemistry, [3]Department of Biophysics, University of Michigan, Ann Arbor, MI 48109 and [4]Center for Theoretical Biological Physics, University of California San Diego, San Diego, CA 92037, USA

Received June 16, 2011; Revised September 19, 2011; Accepted September 20, 2011

ABSTRACT

Single-stranded RNAs (ssRNAs) are ubiquitous RNA elements that serve diverse functional roles. Much of our understanding of ssRNA conformational behavior is limited to structures in which ssRNA directly engages in tertiary interactions or is recognized by proteins. Little is known about the structural and dynamic behavior of free ssRNAs at atomic resolution. Here, we report the collaborative application of nuclear magnetic resonance (NMR) and replica exchange molecular dynamics (REMD) simulations to characterize the 12 nt ssRNA tail derived from the prequeuosine riboswitch. NMR carbon spin relaxation data and residual dipolar coupling measurements reveal a flexible yet stacked core adopting an A-form-like conformation, with the level of order decreasing toward the terminal ends. An A-to-C mutation within the polyadenine tract alters the observed dynamics consistent with the introduction of a dynamic kink. Pre-ordering of the tail may increase the efficacy of ligand binding above that achieved by a random-coil ssRNA. The REMD simulations recapitulate important trends in the NMR data, but suggest more internal motions than inferred from the NMR analysis. Our study unmasks a previously unappreciated level of complexity in ssRNA, which we believe will also serve as an excellent model system for testing and developing computational force fields.

INTRODUCTION

Single-stranded RNAs (ssRNAs), typically located at the ends of RNA hairpins and consisting of more than three unpaired residues, serve diverse structural and functional roles. They can fold onto neighboring RNA hairpins to form pseudoknots, essential architectural RNA elements involved in ribosomal frameshifting (1,2), hepatitis C internal ribosomal entry site (IRES) recognition (3,4) and telomerase activity (5). Messenger RNA (mRNA) degradation is prevented or promoted by 3′ addition of a polyadenylated tail, which recruits essential protein cofactors (6). Cleavage of the 5′ transfer RNA (tRNA) leader by RNase P is a key step in tRNA maturation (7). In riboswitches, ssRNA links the ligand-binding aptamer domain to the expression platform, providing the basis for communication between the two (8–10).

Much of our understanding of the conformational behavior of ssRNA comes from high-resolution NMR and X-ray structures of RNA, in which ssRNA directly engages in tertiary or RNA–protein interactions. However, the atomic-level structural and dynamic behavior of these elements in the absence of these interactions remains unclear, in large part due to their high degree of flexibility. Several studies suggest that ssRNA polynucleotides adopt stacked and partially helical conformations, particularly adenine-rich sequences; however, the biological relevance of these structures is unclear (11–17). Atomic-resolution studies of ssRNA are scarce: at present only one isosequential ssRNA and ssDNA sequence has been characterized by homonuclear NMR methods and shown to possess properties reminiscent of A-form and B-form helices, respectively (18). Few MD studies have been

*To whom correspondence should be addressed. Tel: +734 647 6682; Fax: +1 734 647 1604; Email: brookscl@umich.edu
Correspondence may also be addressed to Hashim M. Al-Hashimi. Tel: +734 615 3361; Fax: +1 734 647 4865; Email: hashimi@umich.edu

The authors wish it to be known that, in their opinion, the first two authors should be regarded as joint First Authors.

© The Author(s) 2011. Published by Oxford University Press.
This is an Open Access article distributed under the terms of the Creative Commons Attribution Non-Commercial License (http://creativecommons.org/licenses/by-nc/3.0), which permits unrestricted non-commercial use, distribution, and reproduction in any medium, provided the original work is properly cited.

Downloaded from http://nar.oxfordjournals.org/ at University of Michigan on February 14, 2012

performed on ssRNA, the majority of which use the AMBER force field (19,20) to explore the impact of chemical modifications such as peptide nucleic acids (PNA) and O2′-methylation (21–24).

The class I prequeuosine riboswitch (*queC*), typically found in firmicute bacterial species, is commonly located in the 5′-untranslated region (UTR) of the queCDEF operon, which expresses proteins directly involved in the queuosine biosynthetic pathway (25). The aptamer binds $preQ_1$, an intermediate in queuosine synthesis, with high affinity to attenuate protein expression at either the transcription or translation level (25). This class has the smallest minimal aptamer domain (34 nucleotides, nt) discovered to date, consisting of a small hairpin followed by a 12 nt ssRNA tail (Figure 1A). Upon ligand recognition, the highly conserved adenine-rich tail condenses into a pseudoknot, forming a host of interactions to both the hairpin and ligand, including A-minor 'kissing' interactions between the ssRNA polyadenine tract and the minor groove (26–30). The activity of transcription-regulating riboswitches, such as the *Bacillus subtilis queC* riboswitch, has been shown to depend on the kinetics of ligand binding as well as the rate of transcription (8). Notably, the very small size of the *queC* riboswitch leaves very little time, in comparison to other switches, for ligand binding to take place prior to formation of the anti-terminator helix which, when formed, prevents terminator helix formation, thereby allowing gene expression to continue. For example, the *B. subtilis* FMN riboswitch, which is highly dependent upon the rate of polymerase and contains sites that locally pause polymerase to lengthen the ligand-binding window, has ~70 nt between the minimal aptamer sequence and complete formation of the anti-terminator helix (8). In comparison, the ligand-binding window for the *queC* riboswitch is ~20 nt (26,27). How efficient ligand binding is achieved is unclear given that the ssRNA tail is thought to be highly disordered, and therefore capable of sampling a wide range of competing conformations.

Here, we use NMR chemical shifts, spin relaxation, and residual dipolar couplings (RDCs) in conjunction with REMD simulations using the recently updated CHARMM27 nucleic acid force field (31,32) to explore the conformational properties of the 12 nt ssRNA tail from the *queC* aptamer domain and the impact of a single A-to-C mutation targeting the polyadenine tract. Our study unmasks a previously unappreciated level of complexity in ssRNA and suggests that these structures can serve as excellent model systems for testing and developing computational force fields.

MATERIALS AND METHODS

Sample preparation

Uniformly $^{13}C/^{15}N$-labeled queC36 and C14U/C17U constructs were prepared by *in vitro* transcription as described previously (33). Unlabeled wild-type (WT, 5′-AUAAAAAACUAA-3′) and A29C (5′-AUAACAAA CUAA-3′) RNAs were purchased from Integrated DNA Technologies (IDT) and purified using a C18 column (Waters) followed by lyophilization and reconstitution in NMR buffer (15 mM sodium phosphate, pH 6.4; 25 mM sodium chloride, 0.1 mM EDTA) containing 10% D_2O by volume. 100% D_2O samples were prepared by repeatedly lyophilizing the sample and replacing with 99.99% pure D_2O (Sigma) three times. RNA concentrations ranged from 1.5 to 2.8 mM. AMP, UMP and CMP (Sigma) were directly dissolved into NMR buffer with no additional purification to 5 mM. For RDC measurements, samples were dialyzed into Millipore-purified ddH_2O using 1 kDa dialysis tubing (Spectrum Labs), lyophilized, and reconstituted into 52.4 mg/ml *Pf1* phage solution (34–36) in NMR buffer with 100% D_2O (Asla Biotech). RNA concentrations in *Pf1* phage ranged from 1.5 to 2 mM.

UV/Vis melting

RNA samples (0.25–0.5 μM) were prepared in NMR buffer and the melting profiles measured between 275 K and 368 K using a Varian Bio 300 UV/Vis instrument equipped with a Cary Temperature Controller. The absorbance at 260 nm was recorded every 0.5° with a ramp rate of 0.5°/min. The two-state helix to coil melting transition was analyzed using

$$A = A_C + \left((A_H - A_C) \frac{e^{\left(\frac{\Delta S}{R} - \frac{\Delta H}{RT}\right)}}{1 + e^{\left(\frac{\Delta S}{R} - \frac{\Delta H}{RT}\right)}} \right),$$

where A is the absorbance value at a given temperature T, A_H is the absorbance of the fully helical ssRNA, A_C is the absorbance of the fully random coil ssRNA, ΔS and ΔH are the entropy and enthalpy of the melting transition respectively, and R is the gas constant (37,38). Absorbance values were fitted to the above equation using the non-linear least squares fitting function in Origin 7 to determine thermodynamic parameters. The melting temperature (T_m) was determined by dividing the enthalpy by the entropy.

NMR experiments

All NMR experiments were performed on a Avance Bruker 600 MHz NMR spectrometer equipped with a triple-resonance 5-mm cryogenic probe. NOESY experiments were performed at 277 K and 298 K using a mixing time of 350 ms (39). ^{13}C spin relaxation experiments were performed at natural abundance and 298 K (40). Relative order parameters were calculated by normalizing ($2R_2$–R_1) to either A31 (C8) or C33 (C6). Relaxation parameters were computed using HydroNMR (41,42), assuming an idealized A-form structure, to obtain diffusion tensor parameters (τ_m and D_{ratio}), and in-house written software was used to compute R_2/R_1 values as previously reported (33,40). Motionally averaged bond lengths of 1.104 Å were used for both C8 and C6 moieties as previously described (40,43). The following experimentally derived CSAs (σ_{xx}, σ_{yy}, σ_{zz}) were used in the analysis: (89, 15, −104); (80, 5, −85); and (98.4, 9.2, −107.5) for C2, C8 and C6 moeties (43,44). IP-COSY experiments were performed at 277 K and 298 K to observe relative $^3J_{H1'-H2'}$ scalar coupling crosspeak intensities (45). Base and sugar ^1H-^{13}C splittings were measured from the

Downloaded from http://nar.oxfordjournals.org/ at University of Michigan on February 14, 2012

difference between the upfield and downfield components of the ^{1}H-^{13}C doublet along the ^{1}H component using the narrow transverse relaxation-optimized spectroscopy (TROSY) component in the ^{13}C dimension as implemented in 2D ^{1}H-^{13}C S^{3}CT-heteronuclear single quantum correlation (HSQC) experiments (46). ^{2}H splittings were 71 and 69 Hz for WT and A29C, respectively. Idealized A-form structures were constructed using Insight II (Molecular Simulations, Inc.) correcting the propeller twist angles from +15° to −15° using an in-house program, as previously described (47). The complementary strand was removed and the resulting ssRNA used in NMR data analysis. B-form helices were constructed using W3DNA (48).

Computational methods

Simulation. REMD simulations were performed with the CHARMM simulation package (49) using the recently updated CHARMM27 nucleic acid force field (31,32) and the MMTSB (50) tool set. Each REMD simulation comprised 40 replicas exponentially distributed over a temperature range from 278 K to 330 K, resulting in an average exchange acceptance ratio of 30%. Each replica was first equilibrated for 0.5 ns, restraining nucleotide heavy atoms, and subsequently run without any restraints for 10 ns, with exchange moves attempted every 0.5 ps.

Both WT and A29C RNAs were initially built in an ideal A-form helical configuration and served as the starting conformation in every simulation of REMD. The RNA was solvated in an 80-Å cubic box of pre-equilibrated TIP3P water (approximately 50 000 atoms). Twelve pairs of sodium chloride with an additional 11 sodium ions were added to the box, corresponding to the experimental ionic concentration of 40 mM.

Analysis. We utilized the last 5 ns of the REMD trajectory at 298 K for the following analysis. Base stacking energies were defined as the electrostatic and van der Waals interaction energies between the adjacent bases. The molecular orientation was expressed by the order parameters S^2 of the C–H bond vectors employing the model-free approach of Lipari and Szabo (51). After a translational and rotational fit of each RNA snapshot to the ideal A-form helical structure, the order parameters were taken from the plateau phase of the correlation function, given by $C(t) = \langle P_2(\vec{\mu}(0) \cdot \vec{\mu}(t)) \rangle$, where P_2 is the second order Legendre polynomial and $\vec{\mu}$ is the unit vector along the C–H dipole. Additionally, from the atomic coordinates we constructed the RDC values by first orienting an idealized A-form ssRNA helix into the principal axis system determined from the order tensor analysis of the experimental RDCs. Each frame of the trajectory was superimposed with this ideal helix followed by calculating the average of , $\left\langle \frac{3\cos^2\theta - 1}{2} \right\rangle$, where θ is the angle between a given bond vector (e.g. C1′H1′) and the z-axis. The RDC values were then scaled by $-82/r^3$, in which r is the C–H bond length and a factor of −82 is applied to shift the computed RDCs to the same scale as the NMR values. The average structure of the ssRNA was calculated as the structure with the minimal root-mean-square deviations from all RNA conformations in the 5 ns REMD trajectory.

RESULTS AND DISCUSSION

NMR chemical shift and NOE-based analysis of the ssRNA tail conformation

Previous studies have shown that in the absence of ligand, the *queC* aptamer domain folds into a non-native hairpin, in which the 5′-strand frame-shifts to allow the first two guanine residues to base pair, with the 12 nt ssRNA tail lacking any tertiary interactions (26). The 2D C–H NMR spectra of the 36 nt *queC* minimal aptamer domain (Figure 1A), in the absence of ligand, show severe resonance overlap and large variations in resonance intensities indicating a highly disordered conformation (Figure 1B). Excess imino proton resonances as well as ^{1}H-^{15}N NOE data indicate that the unbound *queC* aptamer domain is in equilibrium between native and non-native hairpin conformations (data not shown), consistent with previous NMR studies (26).

The NMR spectra suggest that the unbound 36 nt *queC* minimal aptamer domain is highly disordered and that the ssRNA tail is not involved significantly in any tertiary interactions. To test this hypothesis further, we compared NMR spectra of the isolated 12 nt ssRNA tail with the corresponding spectra of the unbound *queC* aptamer. Remarkably, NMR spectra of the isolated 12 nt ssRNA tail overlay almost perfectly with the *queC* aptamer domain and specifically onto the highly intense resonances corresponding to highly disordered residues (Figure 1B). The only significant deviations are observed for A25 and U26, which are located at the junction site between the hairpin and the tail (Figure 1B). This indicates that in the absence of ligand, the ssRNA tail is not involved in any significant tertiary interactions under the NMR conditions

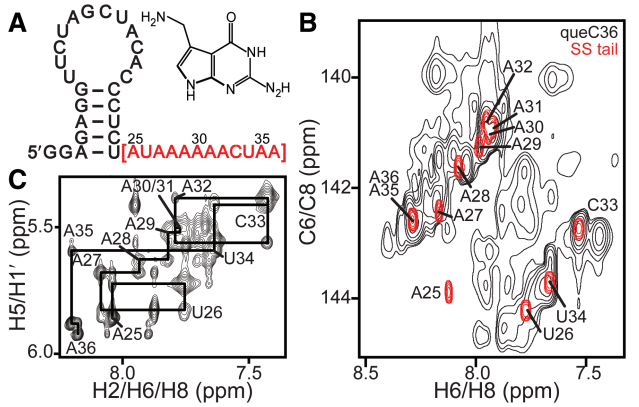

Figure 1. (**A**) Sequence and secondary structure of the *B. subtilis queC* riboswitch minimal aptamer with $PreQ_1$ inset, (**B**) 2D C–H NMR chemical shifts show near-identical agreement between single-stranded tail (SS tail), shown in red, and unbound minimal aptamer (queC36), (**C**) NOE crosspeaks at 277 K enable resonance assignment and indicate base stacking within single strand.

Downloaded from http://nar.oxfordjournals.org/ at University of Michigan on February 14, 2012

(1 mM RNA, 25 mM sodium chloride, 15 mM sodium phosphate, pH 6.4, 0.1 mM EDTA, 298 K).

Similarly to the *Fusobacterium nucleatum queC* riboswitch, the *B. subtilis queC* aptamer forms kissing dimers, as observed in non-denaturing polyacrylamide gels (Supplementary Figure S1) (52). To ensure that the dimer does not obstruct hairpin–tail interactions, we compared a mutant C14U/C17U construct characterized previously by Kang and coworkers to generate a ligand-bound solution NMR structure (26) to the WT aptamer. MFold predicts the C14U/C17U mutations will reduce the dimer stability from −6.1 kcal/mol to −0.9 kcal/mol (53). While we observe removal of the kissing dimer, chemical shifts overall overlay extremely well between the WT *queC* aptamer and the C14U/C17U mutant (Supplementary Figure S1). Specifically, tail chemical shifts correspond extremely well to the 12 nt ssRNA, further suggesting that the tail does not participate in tertiary interactions in the absence of ligand under our NMR conditions.

Strikingly, the spectra of the 12 nt ssRNA are well resolved, indicating that it does not adopt a completely random conformation (Figure 1B and Supplementary Figure S2). This stands in stark contrast to corresponding spectra of a 12 nt polyuridine (polyU) ssRNA, well established to have a random-coil conformation (16), which exhibits severe spectral overlap indicative of a highly disordered conformation (Supplementary Figure S2). This structural order is observed in the ssRNA despite the lack of any observable imino protons and therefore any base pairing or secondary structure (Supplementary Figure S3).

The 2D ^{1}H–^{1}H NOESY spectrum of the ssRNA shows abundant nuclear Overhauser effect (NOE) connectivities expected for a helical conformation, allowing the near complete assignment of base and sugar (H1′) protons at 298 K (Supplementary Figure S3). Particularly noteworthy are inter-base NOEs observed between adenine H8 protons within the polyadenine tract and between C33-U34 H6 protons, indicating significant base stacking within the polyadenine core at 277 K and decreased at 298 K (Supplementary Figure S3) (54). Sequential NOEs are only observed for A25, U26, A35, and A36 upon decreasing the temperature from 298 K to 277 K, indicating a higher level of disorder at the terminal ends (Figure 1C and Supplementary Figure S3). Furthermore, homonuclear three bond scalar couplings ($^{3}J_{H1'-H2'}$) indicate that residues within the polyadenine core adopt a C3′-endo sugar pucker conformation, consistent with an A-form-like geometry, with the tendency to adopt alternative sugar pucker conformations increasing towards terminal residues (Supplementary Figure S2).

NMR chemical shifts are extremely sensitive probes of the local electronic environment for a given bond vector and can provide useful structural information (55–58). Highly disordered residues are expected to have chemical shifts similar to nucleotide monophosphates (NMPs). While the chemical shifts of terminal residues are similar to their NMP analogs, increasing differences are observed when approaching the polyadenine core with the greatest differences observed for A30–32 (Supplementary Figure S2). The directionality of the chemical shifts is consistent with increased formation of stacking interactions towards the center of the tail (57). This is further supported by chemical shift perturbations in a trajectory toward the NMPs with increasing temperature (data not shown). Alternatively, addition of magnesium up to 4 mM results in slight chemical shift perturbations farther from NMPs, consistent with previous studies suggesting that increases in ionic strength stabilize ssRNA stacking interactions (59) (data not shown). In contrast polyU has near-identical (≤0.1 ppm) chemical shifts to UMP (Supplementary Figure S2). Thus, consistent with NOE data, the chemical shift data suggest a comparatively stacked core with a growing level of disorder towards the terminal ends. Normalized resonance intensities (33) further support these observations, which gradually increase towards the terminal ends, consistent with a higher level of pico- to nanosecond motions (Supplementary Figure S2).

Thermal stability by experiment and REMD computation

The abundance of NOEs indicates significant base stacking interactions, which likely contribute to ordering of the tail. To probe the thermodynamic stability of the tail, we performed UV/Vis melting experiments to determine the melting temperature of the helix to coil transition. Consistent with previous studies of single-stranded nucleic acids, the melting profile of the ssRNA is extremely broad, characteristic of a non-cooperative transition (Figure 2A) (37). Previous studies of a 7 nt polyadenine ssRNA in similar buffer conditions yield analogous melting temperatures to those observed (∼35°C compared to 31.7 ± 1.90°C) (37).

We then used our REMD simulations to explore the temperature dependence of base stacking compared to the described UV/Vis melting curves. Base stacking energies from the REMD simulation between temperatures 278–330 K show a similar gradual decrease with increasing temperature and a similar, although reduced, T_m value (experimental 31.7 ± 1.90°C compared

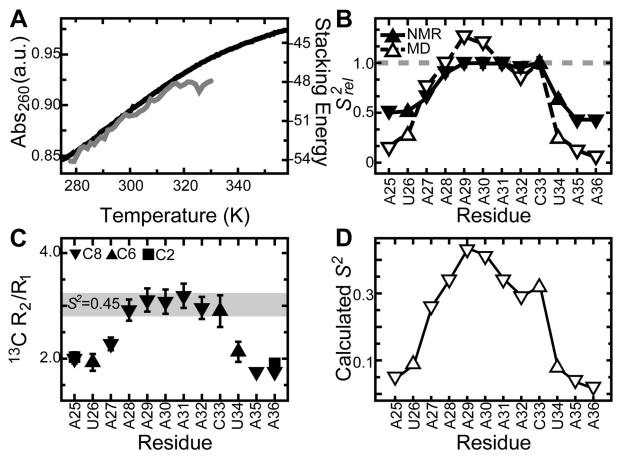

Figure 2. (**A**) UV melting profile (black) compared to base stacking energy calculated from REMD simulations (gray), (**B**) NMR (closed) and REMD (open) relative order parameters suggest central polyadenine residues are more ordered with flexible terminal ends, (**C**) NMR ^{13}C spin relaxation R_2/R_1 values, with HYDRONMR-predicted values assuming an order parameter (S^2) of 0.45 shown as a gray bar, (**D**) REMD-calculated order parameters.

Downloaded from http://nar.oxfordjournals.org/ at University of Michigan on February 14, 2012

to computed 20–25°C, as estimating the T_{50} value from melting curve, Figure 2A). However, the calculated base stacking energy plateaus around 320 K while the experimental slope begins to plateau around 330 K, indicating that stacking energies may be under-estimated in the REMD simulation or that additional unaccounted-for factors contribute to the ssRNA stability. Nevertheless, our data suggest that base stacking is the guiding force behind ssRNA stability, consistent with previous studies.

Picosecond to nanosecond dynamics by NMR spin relaxation and comparison with REMD simulations

To gain further insights into the dynamic properties of the ssRNA at pico- to nanosecond timescales, we measured longitudinal (R_1) and transverse (R_2) carbon relaxation data for the nucleobases (C2 C6 C8) using 2D ^{13}C relaxation R_1 and $R_{1\rho}$ NMR experiments (40), where R_1 and R_2 values are determined using in-house software (Supplementary Figure S4). These measurements represent the first nucleobase ^{13}C relaxation measurements performed on a ssRNA. The measured R_1 and R_2 values were used to compute order parameters (51) using $S^2 = (2R_2–R_1)$ (60), and normalized to yield a relative order parameter (S^2_{rel}) describing the relative degree of order within a molecule ranging from 0 to 1, where 0 and 1 represent minimum and maximum order, respectively. The S^2_{rel} values were normalized against central residues A31 (C8) and C33 (C6). Resonance overlap prevented the normalization of C2 spins. Again, we observe a gradual reduction in S^2_{rel} indicating higher levels of disorder moving from central polyadenine residues (A28–C33) towards the terminal ends (Figure 2B).

We also computed the S^2_{rel} values based on the REMD simulation described above. The REMD simulations reproduce the general trends observed in the experiments; however, the simulations show significantly increased dynamics at the terminal ends compared to experimental values, with S^2_{rel} values approaching the dynamic limit (Figure 2B). Additionally, while experimental values have similar relative order parameters from A28–C33, large variations are observed in the REMD simulation, with A29–A30 being more ordered and A32 less ordered than experimentally observed (Figure 2B). These differences may reflect shortcomings in the force field and/or mismatch in the experimental/computational timescales since the REMD simulations likely probe fluctuations that extend beyond the picosecond timescales sensed by spin relaxation data.

The high level of disorder and motional coupling in the ssRNA prevents quantitative analysis of relaxation data using the model-free formalism, which assumes that internal and overall motions are decoupled from one another (51). This makes it difficult if not impossible to assess the absolute level of disorder in the ssRNA; one can only make qualitative assessments about the relative disorder across different residues. However, it is noteworthy that even the comparatively high R_2/R_1 values measured in the rigid core (~2.9, Figure 2C) remain significantly lower than values predicted for a perfectly rigid helical ssRNA (~6.4, Supplementary Figure S4) as estimated using the program HYDRONMR (41,42). If we assume an overall diffusion tensor predicted by HYDRONMR, we find that central polyadenine residues are highly flexible with an estimated average NMR spin relaxation order parameter S^2 of ~0.45 (Figure 2C and Supplementary Figure S4). Interestingly, similar though slightly smaller absolute S^2 values are calculated from the REMD simulations (on average $S^2 \sim 0.36$ for core residues, Figure 2D). These data indicate that despite measurable stacking interactions and a helical-like average conformation, the polyadenine core is highly disordered with residues experiencing fluctuations on the order of a $\pm 40°$ cone angle (61) at pico- to nanosecond timescales.

Overall conformation and sub-millisecond dynamics by NMR residual dipolar couplings and comparison with REMD simulations

To further probe the conformation of the ssRNA and extend the NMR timescale sensitivity to milliseconds, we measured RDCs (62,63) using 52.4 mg/ml *Pf1* phage as an ordering medium. While most RNAs align optimally in ~25 mg/ml of phage, a much higher concentration of phage was used for the ssRNA to ensure optimal alignment. To our knowledge, these are the first RDC measurements reported on a single-stranded nucleic acid. The RDCs measured between two nuclei depend on $\left\langle \frac{3\cos^2\theta - 1}{2} \right\rangle$, where θ is the angle between the inter-nuclear vector and the magnetic field and the angular bracket denotes a time-average over all orientations sampled at sub-millisecond timescales (62,63). RDCs were measured for base C5H5, C6H6, C8H8, C2H2 and sugar C1′H1′ moieties (47).

In general, isotropic motions tend to reduce the observed RDC value, approaching zero at the limit of spatially unrestricted isotropic motions (61,64,65). In the ssRNA, large base C–H RDCs are measured in the polyadenine tract residues that gradually decrease at the termini (Figure 3A). Although small RDC values can also arise from static placement of the bond vector near the magic angle relative to the principal direction of order, the overall trends observed are consistent with NMR chemical shift and S^2_{rel} data suggesting that the RDCs indicate increased dynamic averaging at the termini (Figure 3A). Interestingly, the near-zero RDCs measured at terminal residues (Figure 3A and Supplementary Figure S5) agree more closely to the REMD simulations compared to the S^2_{rel} values, indicating that the discrepancy between the measured and computed S^2_{rel} values may be due to truncation of the S^2 sensitivity to motions faster than nanoseconds. These results add to a growing number of NMR studies on different types of RNA showing that RDC data are capable of probing motions that are incompletely sensed by spin relaxation due to truncation of the time-sensitivity by overall correlation time of the molecule (64,66–68). Unfortunately, severe spectral overlap, particularly pronounced in the *Pf1* phage sample, prevented measurement of several C1′H1′ RDCs for the polyadenine core.

We subjected the RDCs (excluding RDCs for the two flexible residues from the terminal ends) to an order tensor

Downloaded from http://nar.oxfordjournals.org/ at University of Michigan on February 14, 2012

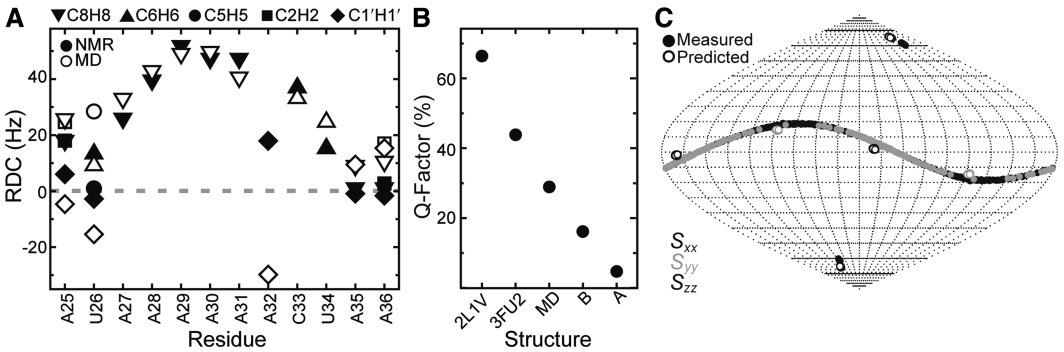

Figure 3. RDCs and order tensor analysis of the 12 nt *queC* aptamer tail (**A**) Measured (closed) and computed (open) RDCs show reduced values at the terminal ends, indicating increased dynamics, (**B**) Q-factor comparison indicates the ssRNA adopts an A-form conformation, (**C**) Sauson-Flamsteed map shows good agreement between predicted (open) and experimental (closed) order tensors.

analysis (47,69,70) assuming different input structures including single strands derived from idealized A-form and B-form helices, the REMD-averaged structure, and available ligand-bound X-ray and NMR structures (26,27). Despite the relatively small number of RDCs used in this analysis, we clearly observe a better fit with an A-form geometry (Q-factor 4.77%) as compared to all other conformations (Q-factor $\geq$ 16%) (Figure 3B). This is consistent with independently observed $^{3}J_{H1'-H2'}$ scalar coupling crosspeaks, which indicate a C3′-endo sugar conformation for core residues in the tail, suggesting an A-form (and not B-form) helical geometry. The RDCs are in strong disagreement with preQ$_1$-bound X-ray and NMR structures (PDBID: 3FU2 and 2L1V) indicating that the tail must undergo a transition from an A-form helical geometry towards the distinct helical conformation observed in the X-ray and NMR structures in which the A-form geometry is perturbed at the hairpin-tail junction, likely due to torsional strain from the ssRNA folding back upon the hairpin. The REMD-averaged structure has a Q-factor of 30%, indicating a better fit than ligand-bound structures, but is still outside the range considered to represent a good fit. Together, these data suggest that, on average, the ssRNA tail adopts an A-form like conformation. The good RDC fit to the A-form structure also suggests that averaging of the RDCs due to internal motions is largely isotropic in nature, causing a semi-uniform attenuation of the RDCs relative to values expected for an A-form structure. The dynamics could involve exchange between a stacked ordered conformation and unstacked highly disordered conformation, or local isotropic motions about the average A-form conformation.

As a further check on the accuracy of the A-form structure, we compared the principal direction of alignment (S_{zz}) determined experimentally using RDCs assuming a ssRNA A-form structure with the orientation predicted by PALES (71) using a ssRNA A-form structure. Surprisingly, we find that the experimentally determined S_{zz} deviates from the helix axis by ~19.8° (Figure 3C). Interestingly, PALES predicts a principal direction of order that deviates from the helix axis by 14.4°; the S_{zz} orientation predicted using PALES is in good agreement from that measured experimentally (deviation ~5°). The deviation from the helix axis can be attributed to the absence of the complementary strand, resulting in an overall shape with a long axis that is not coincident with the helical axis, as reported previously for a quadruplex DNA topology (72).

To further test the conformational distribution from the REMD simulations, we used a number of simplifying assumptions to compute RDCs from the REMD trajectory. Snapshots from the REMD simulations were superimposed onto an idealized A-form helix oriented in the principal axis system determined using the experimental RDCs and the order tensor fit. RDCs were then arbitrarily scaled by $-82/r^3$, in which r is the C–H bond length and accounts for bond length variations during the dynamics. We find excellent agreement between experimental and computed nucleobase RDCs; however, computed C1′H1′ RDCs fail to reproduce observed RDCs, particularly for A32: while the magnitude is similar (18 Hz compared to −30 Hz) the sign differs, suggesting the orientation of the C1′H1′ bond vector differs between experiment and simulation (Supplementary Figure S5). C1′H1′ RDCs are generally opposite in sign to base RDCs in a double-stranded A-form helix. However, back-calculated C1′H1′ RDCs from the order tensor analysis assuming a ssRNA A-form helix are positive in sign, suggesting the C1′H1′ orientation in the REMD simulations deviates from an A-form structure (Supplementary Figure S5).

Impact of A-to-C mutation within polyadenine core

Taken together, the data show that the polyadenine tract is relatively ordered at 298 K, with a gradual reduction in order approaching the termini and that the base stacking interactions are the guiding force behind this order. To determine whether disrupting the polyadenine tract will destabilize the global structure, we substituted A29 within the polyadenine tract with a cytosine residue (referred to as A29C). Other types of mutations involving placements of uridine were not explored as these were expected to yield partially base paired conformations. As with the WT construct, we observed no imino protons, indicating the absence of any detectable base pairing and secondary structure (Supplementary Figure S7).

Downloaded from http://nar.oxfordjournals.org/ at University of Michigan on February 14, 2012

The 2D C–H spectra for the A29C mutant remain highly disperse, and the chemical shift perturbations relative to WT are clustered around the site of mutation (A28 and A30) (Figure 4A and Supplementary Figure S6). However, small but significant chemical shift perturbations relative to WT are also observed at more distant residues, including A27, A31, C33 and U34. These perturbations diminish when moving away from the center of the ssRNA and are basically absent in the highly flexible terminal residues (Figure 4A and Supplementary Figure S6). Such longer-range perturbations suggest that the mutation may have a long-range effect possibly by influencing the stacking interactions of several nucleobases. A perturbation to stacking interactions is also supported by distinct NOE connectivities in A29C, which show weakened cross peaks to C29, and new crosspeaks between A28 (H2) and A30 (H1′) that indicate C29 partially loops out to allow A28 to stack onto A30 (Supplementary Figure S7). The melting temperature of the mutant is reduced by ~5°C, and the base stacking energies are computed to be ~2 kcal/mol lower compared to WT, indicating that the mutation likely destabilizes the stacking interactions (Supplementary Figure S6).

Interestingly, many of the residues that experience chemical shift perturbations following the A29 to C29 mutation also exhibit a greater degree of dynamics as assessed by normalized resonance peak intensities in 2D C–H HSQC spectra (Supplementary Figure S6) and carbon relaxation data (R_1 and R_2) (Figure 4B and Supplementary Figure S8). In particular, severe line broadening consistent with a slow exchange process occurring at micro- to millisecond timescales manifesting as reduced resonance intensities in 2D spectra and higher R_2 values

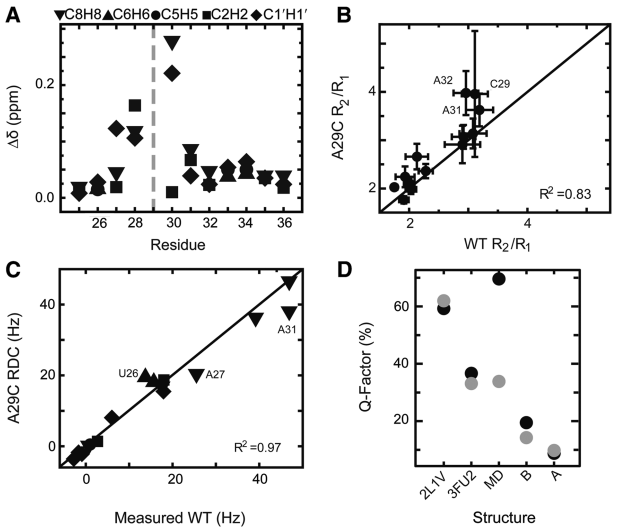

Figure 4. Comparison of WT and A29C constructs (**A**) Chemical shift perturbations between WT and A29C are largely localized about mutation site, (**B**) NMR spin relaxation parameters between WT and A29C are similar, with deviations occurring several residues from mutation site, (**C**) Measured RDCs between WT and A29C values show good agreement, (**D**) Q-factor indicates A29C adopts A-form conformation. Gray circles indicate quality of fit upon removal of A28 C8H8, A30 C1′H1′ and A30 C2H2 measured NMR values from order tensor analysis.

is observed for C29 in the A29C mutant (Supplementary Figures S6 and S8). This is not observed for A29 in WT. Smaller but significant line broadening is also observed for residues A31, A32 and U34 (Supplementary Figure S8). This line broadening across several residues may reflect exchange between stacked and unstacked conformations. Higher intensities as well as reduced S^2_{rel} values are observed for residues A27 and A28, indicating a greater degree of fast pico- to nanosecond dynamics (Supplementary Figures S6 and S8). Note that the high R_2 and weak signal intensity leads to a higher error in the R_2/R_1 measurements, particularly for C29.

Although the A29C RDCs are generally in good agreement with the WT RDCs, variations are observed for a number of residues (U26, A27, A31) that indicate differences in conformation and/or dynamic behavior (Figure 4C). Though an order tensor analysis of 13 RDCs shows best agreement with an A-form structure, the quality of the fit is not as good as that observed for WT (Q-factor = 8.77%, Figure 4D). The S_{zz} direction measured for A29C when assuming an A-form structure deviates substantially from that predicted using PALES (~11°, Supplementary Figure S9). These data suggest that A29C deviates from an idealized A-form structure as compared to WT. These deviations may reflect static and/or dynamic bending about the C29 pivot point, possibly arising from looping out of this residue from the helical stack. Such a conformation is observed in the REMD simulations of A29C ~1% but not in WT (data not shown).

In general, the REMD simulations predict the NMR data measured for A29C with reduced quality to that noted for WT. Interestingly, the computed absolute S^2 values indicate a global reduction in order for A29C, particularly for residues A27–C33 (Supplementary Figure S8), whereas NMR relaxation parameters between WT and A29C are more similar, suggesting comparable global order parameters. The REMD simulations reveal enhanced dynamics at C29 consistent with the NMR chemical exchange data. The REMD simulation also suggests increased dynamics at A32, which is not observed experimentally: although slightly reduced, the S^2_{rel} is within error of A29–A31 values (S^2_{rel} of 1) (Supplementary Figure S8). Computed RDCs agree reasonably with measured RDCs, although the C1′H1′ RDCs are opposite in sign as observed in the comparison between WT NMR and REMD-calculated RDCs. The Q-factor comparing the average REMD structure to measured RDCs is 70%; however, removal of A28 C8H8, A30 C2H2 and A30 C1′H1′ RDCs improves the Q-factor significantly. This improvement is observed only for the REMD structure (Figure 4D), indicating that these residues, localized about the mutation site, adopt non-A-form conformations and likely experience perturbations from the increased dynamics at C29. The difference in timescales between the REMD simulations and NMR may be another factor leading to the observed discrepancies. Nevertheless, MD and NMR data both indicate significant dynamics at the mutation site with perturbations extending toward the 3′ end of the ssRNA.

Downloaded from http://nar.oxfordjournals.org/ at University of Michigan on February 14, 2012

ssRNA tail conformation and dynamics optimized for ligand docking in *queC* aptamer

One of the main questions we set out to explore during the course of our studies was how the *queC* aptamer manages to efficiently bind its cognate ligand despite the small commitment time available in the kinetic switch and the large conformational space that may be available to a highly disordered ssRNA, which would have to search many competing conformations before arriving at the ligand bound pseudoknot conformation. Our study reveals that the ssRNA is not entirely disordered, but rather, has the character of a stacked A-form-like helical conformation which may effectively reduce the conformational search of the ssRNA, promoting efficient docking onto the hairpin to form the pseudoknot. Moreover, our study uncovers a greater degree of flexibility towards the terminal ends, particularly the 5′-end which forms the pivot point for docking the ssRNA tail onto the hairpin.

The NMR data clearly show the absence of any pre-existing tertiary interactions involving the ssRNA tail in the unbound *queC* aptamer domain. This together with our findings regarding the conformational behavior of the unbound ssRNA tail suggests the following model for ligand binding (Figure 5). In the absence of ligand, the ssRNA tail is disordered but on average forms an A-form helix-like conformation, which can efficiently explore conformational space about a highly flexible junction. The ligand may transiently form encounter complexes when the tail is close in space to the P1 hairpin, and possibly with the help of divalent ions such as calcium (27,73), triggering the necessary conformational changes required to form the pseudoknot and binding pocket. This finding is consistent with computational modeling of the ligand binding mechanism in which A-minor tertiary interactions form first, followed by pseudoknot formation (30) and may explain the fast ligand binding rate observed in the related *F. nucleatum queC* riboswitch (52). Our results, including the observation of greater dynamics in the mutant, provide a framework for more rigorous testing of this proposed model with future *in vitro* and *in vivo* studies.

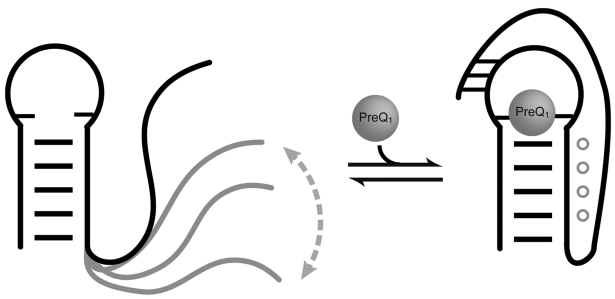

Figure 5. A tentative model for *queC* riboswitch ligand recognition. In the absence of ligand the ssRNA tail rotates freely about the helix-tail pivot point in a stacked, A-form helical-like conformation. Upon ligand recognition the pseudoknot is stabilized. A-minor tertiary interactions are shown as open gray circles.

CONCLUSION

Our study shows that ssRNA can exhibit complex conformational behavior, including variable levels of stacking and propensities to form an A-form helical conformation across the polynucleotide chain, and also, the ability to interrupt stacked residues by introducing sequence-specific kinks and/or distortions. While it has been known for some time that polyadenine stretches tend to stack and form helical conformations (13,14,16,18,37), the details of this helical geometry were difficult to decipher based solely on NOE-based NMR data. Our RDC measurements on the ssRNA, together with scalar coupling constant measurements, strongly suggest that the polyadenine tract forms an A-form-like conformation in the WT ssRNA. Our results also unveil dynamic complexity in ssRNA, including a gradual increase in disorder occurring towards the terminal ends that is reminiscent of unfolded polypeptide chains (74), and also, slower sequence-specific dynamics occurring at micro- to millisecond timescales that may involve transient stacking/unstacking motions that may result in kinking of the ssRNA. Altogether, our studies show that 'structured' ssRNA exhibits exquisite quality spectra and can be studied quantitatively using NMR-based structure and dynamics measurements.

The REMD simulations recapitulate many of the key features and trends observed based on the melting and NMR data, including the existence of stacking interactions that are weakened by the A29C mutation, the formation of helical geometry that may be kinked in A29C at the mutation site, and an increase in dynamic disorder towards the terminal ends and localized about C29 in the mutant. However, the REMD simulations showed weaker agreement with sugar RDCs or sugar conformation, particularly in the A29C mutant, and had increased dynamics compared to the NMR data. Prior studies on HIV-1 TAR RNA noted higher levels of dynamics in CHARMM simulations compared to NMR measurements (75). Our studies indicate that suboptimal base stacking energies may be a source of these excess dynamics. However, a quantitative assessment of the simulations requires the application of domain-elongation methods to rigorously decouple internal and overall motions, and make it possible to quantitatively predict NMR measurements (33,75–77). In addition, MD simulations that retain aspects of time are required to compare the rates of dynamics observed by relaxation and exchange broadening type measurements. The simplicity of ssRNA offers a much needed model system for such studies directed at rigorously examining currently used nucleic acid force fields.

Finally, our results suggest that the conformational properties of the ssRNA tail are optimized to allow the *queC* riboswitch to efficiently bind ligands within the short commitment time available to this kinetic switch. In particular, the pre-stacked ssRNA tail can efficiently rotate about a flexible hinge against the hairpin loop, and explore conformational space efficiently for rapid ligand binding. This pre-stacking about dynamic hinges may be a

Downloaded from http://nar.oxfordjournals.org/ at University of Michigan on February 14, 2012

general feature of many ssRNAs that can play different architectural roles in a variety of RNA contexts.

SUPPLEMENTARY DATA

Supplementary Data are available at NAR Online: Supplementary Figures S1–S9.

ACKNOWLEDGEMENTS

C.D.E. and H.M.A. thank members of the Al-Hashimi lab for insightful discussions and Dr Alex Kurochkin for his expertise and maintenance of the NMR instruments. The authors gratefully acknowledge the Michigan Economic Development Cooperation and the Michigan Technology Tri-Corridor for support in the purchase of the 600 MHz spectrometer.

FUNDING

National Science Foundation (0644278 to H.M.A., PHY0216576 to C.L.B.); National Institutes of Health (RR012255 to C.L.B.). Funding for open access charge: National Science Foundation (0644278).

Conflict of interest statement. H.M.A. is an advisor to and holds an ownership interest in Nymirum Inc., which is an RNA-based drug discovery company. The research reported in this article was performed by the University of Michigan faculty and students and was funded by a NSF contract to H.M.A.

REFERENCES

1. Brierley,I., Digard,P. and Inglis,S.C. (1989) Characterization of an efficient coronavirus ribosomal frameshifting signal: requirement for an RNA pseudoknot. *Cell*, **57**, 537–547.
2. Brierley,I., Rolley,N.J., Jenner,A.J. and Inglis,S.C. (1991) Mutational analysis of the RNA pseudoknot component of a coronavirus ribosomal frameshifting signal. *J. Mol. Biol.*, **220**, 889–902.
3. Rijnbrand,R., van der Straaten,T., van Rijn,P.A., Spaan,W.J. and Bredenbeek,P.J. (1997) Internal entry of ribosomes is directed by the 5′ noncoding region of classical swine fever virus and is dependent on the presence of an RNA pseudoknot upstream of the initiation codon. *J. Virol.*, **71**, 451–457.
4. Wang,C., Le,S.Y., Ali,N. and Siddiqui,A. (1995) An RNA pseudoknot is an essential structural element of the internal ribosome entry site located within the hepatitis C virus 5′ noncoding region. *RNA*, **1**, 526–537.
5. Gilley,D. and Blackburn,E.H. (1999) The telomerase RNA pseudoknot is critical for the stable assembly of a catalytically active ribonucleoprotein. *Proc. Natl Acad. Sci. USA*, **96**, 6621–6625.
6. Lange,H., Sement,F.M., Canaday,J. and Gagliardi,D. (2009) Polyadenylation-assisted RNA degradation processes in plants. *Trends Plant Sci.*, **14**, 497–504.
7. Kurz,J.C. and Fierke,C.A. (2000) Ribonuclease P: a ribonucleoprotein enzyme. *Curr. Opin. Chem. Biol.*, **4**, 553–558.
8. Wickiser,J.K., Winkler,W.C., Breaker,R.R. and Crothers,D.M. (2005) The speed of RNA transcription and metabolite binding kinetics operate an FMN riboswitch. *Mol. Cell.*, **18**, 49–60.
9. Montange,R.K. and Batey,R.T. (2008) Riboswitches: emerging themes in RNA structure and function. *Annu. Rev. Biophys.*, **37**, 117–133.
10. Breaker,R.R. (2010) Riboswitches and the RNA World. *Cold Spring Harb Perspect Biol* (doi:10.1101/cshperspect.a003566; 24 November 2011, epub ahead of print).
11. Fasman,G.D., Lindblow,C. and Grossman,L. (1964) The helical conformations of polycytidylic acid: studies on the forces involved. *Biochemistry*, **3**, 1015–1021.
12. McDonald,C.C., Phillips,W.D. and Penman,S. (1964) Nucleic acids: a nuclear magnetic resonance study. *Science*, **144**, 1234–1237.
13. Brahms,J., Michelson,A.M. and Van Holde,K.E. (1966) Adenylate oligomers in single- and double-strand conformation. *J. Mol. Biol.*, **15**, 467–488.
14. Leng,M. and Felsenfeld,G. (1966) A study of polyadenylic acid at neutral pH. *J. Mol. Biol.*, **15**, 455–466.
15. BouchemalChibani,N., duPenhoat,C.H., Abdelkafi,M., Ghomi,M. and Turpin,P.Y. (1996) Characterization of the dynamic behavior of r(ACC) and r(AAC) with NMR relaxation data and both Metropolis Monte Carlo and molecular dynamics simulations. *Biopolymers*, **39**, 549–571.
16. Seol,Y., Skinner,G.M. and Visscher,K. (2004) Elastic properties of a single-stranded charged homopolymeric ribonucleotide. *Phys. Rev. Lett.*, **93**, 118102.
17. Seol,Y., Skinner,G.M., Visscher,K., Buhot,A. and Halperin,A. (2007) Stretching of homopolymeric RNA reveals single-stranded helices and base-stacking. *Phys. Rev. Lett.*, **98**, 158103.
18. Isaksson,J., Acharya,S., Barman,J., Cheruku,P. and Chattopadhyaya,J. (2004) Single-stranded adenine-rich DNA and RNA retain structural characteristics of their respective double-stranded conformations and show directional differences in stacking pattern. *Biochemistry*, **43**, 15996–16010.
19. Kollman,P.A., Wang,J.M. and Cieplak,P. (2000) How well does a restrained electrostatic potential (RESP) model perform in calculating conformational energies of organic and biological molecules? *J. Comput. Chem.*, **21**, 1049–1074.
20. Perez,A., Marchan,I., Svozil,D., Sponer,J., Cheatham,T.E. III, Laughton,C.A. and Orozco,M. (2007) Refinement of the AMBER force field for nucleic acids: improving the description of alpha/gamma conformers. *Biophys. J.*, **92**, 3817–3829.
21. Kaukinen,U., Venalainen,T., Lonnberg,H. and Perakyla,M. (2003) The base sequence dependent flexibility of linear single-stranded oligoribonucleotides correlates with the reactivity of the phosphodiester bond. *Org. Biomol. Chem.*, **1**, 2439–2447.
22. Yeh,I.C. and Hummer,G. (2004) Diffusion and electrophoretic mobility of single-stranded RNA from molecular dynamics simulations. *Biophys. J.*, **86**, 681–689.
23. Biyani,M. and Nishigaki,K. (2005) Single-strand conformation polymorphism (SSCP) of oligodeoxyribonucleotides: an insight into solution structural dynamics of DNAs provided by gel electrophoresis and molecular dynamics simulations. *J. Biochem.*, **138**, 363–373.
24. Panecka,J., Mura,C. and Trylska,J. (2011) Molecular dynamics of potential rRNA binders: single-stranded nucleic acids and some analogues. *J. Phys. Chem. B*, **115**, 532–546.
25. Roth,A., Winkler,W.C., Regulski,E.E., Lee,B.W., Lim,J., Jona,I., Barrick,J.E., Ritwik,A., Kim,J.N., Welz,R. *et al.* (2007) A riboswitch selective for the queuosine precursor preQ1 contains an unusually small aptamer domain. *Nat. Struct. Mol. Biol.*, **14**, 308–317.
26. Kang,M., Peterson,R. and Feigon,J. (2009) Structural Insights into riboswitch control of the biosynthesis of queuosine, a modified nucleotide found in the anticodon of tRNA. *Mol. Cell.*, **33**, 784–790.
27. Klein,D.J., Edwards,T.E. and Ferre-D'Amare,A.R. (2009) Cocrystal structure of a class I preQ1 riboswitch reveals a pseudoknot recognizing an essential hypermodified nucleobase. *Nat. Struct. Mol. Biol.*, **16**, 343–344.
28. Rieder,U., Lang,K., Kreutz,C., Polacek,N. and Micura,R. (2009) Evidence for pseudoknot formation of class I preQ1 riboswitch aptamers. *Chembiochem*, **10**, 1141–1144.
29. Spitale,R.C., Torelli,A.T., Krucinska,J., Bandarian,V. and Wedekind,J.E. (2009) The structural basis for recognition of the PreQ0 metabolite by an unusually small riboswitch aptamer domain. *J. Biol. Chem.*, **284**, 11012–11016.

Downloaded from http://nar.oxfordjournals.org/ at University of Michigan on February 14, 2012

30. Feng,J., Walter,N.G. and Brooks,C.L. III (2011) Cooperative and directional folding of the preQ1 riboswitch aptamer domain. *J. Am. Chem. Soc.*, **133**, 4196–4199.
31. Denning,E.J., Priyakumar,U.D., Nilsson,L. and Mackerell,A.D. Jr (2011) Impact of 2′-hydroxyl sampling on the conformational properties of RNA: Update of the CHARMM all-atom additive force field for RNA. *J. Comput. Chem.*, **32**, 1929–1943.
32. Foloppe,N. and MacKerell,A.D. (2000) All-atom empirical force field for nucleic acids: I. Parameter optimization based on small molecule and condensed phase macromolecular target data. *J. Comput. Chem.*, **21**, 86–104.
33. Zhang,Q., Sun,X., Watt,E.D. and Al-Hashimi,H.M. (2006) Resolving the motional modes that code for RNA adaptation. *Science*, **311**, 653–656.
34. Clore,G.M., Starich,M.R. and Gronenborn,A.M. (1998) Measurement of residual dipolar couplings of macromolecules aligned in the nematic phase of a colloidal suspension of rod-shaped viruses. *J. Am. Chem. Soc.*, **120**, 10571–10572.
35. Hansen,M.R., Hanson,P. and Pardi,A. (2000) Filamentous bacteriophage for aligning RNA, DNA, and proteins for measurement of nuclear magnetic resonance dipolar coupling interactions. *Methods Enzymol.*, **317**, 220–240.
36. Hansen,M.R., Mueller,L. and Pardi,A. (1998) Tunable alignment of macromolecules by filamentous phage yields dipolar coupling interactions. *Nat. Struct. Biol.*, **5**, 1065–1074.
37. Dewey,T.G. and Turner,D.H. (1979) Laser temperature-jump study of stacking in adenylic acid polymers. *Biochemistry*, **18**, 5757–5762.
38. Freier,S.M., Hill,K.O., Dewey,T.G., Marky,L.A., Breslauer,K.J. and Turner,D.H. (1981) Solvent effects on the kinetics and thermodynamics of stacking in poly(cytidylic acid). *Biochemistry*, **20**, 1419–1426.
39. Hwang,T.L. and Shaka,A.J. (1995) Water suppression that works - excitation sculpting using arbitrary wave-forms and pulsed-field gradients. *J. Magn. Reson. Ser. A*, **112**, 275–279.
40. Hansen,A.L. and Al-Hashimi,H.M. (2007) Dynamics of large elongated RNA by NMR carbon relaxation. *J. Am. Chem. Soc.*, **129**, 16072–16082.
41. Garcia de la Torre,J., Huertas,M.L. and Carrasco,B. (2000) HYDRONMR: prediction of NMR relaxation of globular proteins from atomic-level structures and hydrodynamic calculations. *J. Magn. Reson.*, **147**, 138–146.
42. Bernado,P., Garcia de la Torre,J. and Pons,M. (2002) Interpretation of 15N NMR relaxation data of globular proteins using hydrodynamic calculations with HYDRONMR. *J. Biomol. NMR*, **23**, 139–150.
43. Ying,J., Grishaev,A., Bryce,D.L. and Bax,A. (2006) Chemical shift tensors of protonated base carbons in helical RNA and DNA from NMR relaxation and liquid crystal measurements. *J. Am. Chem. Soc.*, **128**, 11443–11454.
44. Stueber,D. and Grant,D.M. (2002) 13C and (15)N chemical shift tensors in adenosine, guanosine dihydrate, 2′-deoxythymidine, and cytidine. *J. Am. Chem. Soc.*, **124**, 10539–10551.
45. Xia,Y., Legge,G., Jun,K.Y., Qi,Y., Lee,H. and Gao,X. (2005) IP-COSY, a totally in-phase and sensitive COSY experiment. *Magn. Reson. Chem.*, **43**, 372–379.
46. Meissner,A. and Sorensen,O.W. (1999) The role of coherence transfer efficiency in design of TROSY-type multidimensional NMR experiments. *J. Magn. Reson.*, **139**, 439–442.
47. Bailor,M.H., Musselman,C., Hansen,A.L., Gulati,K., Patel,D.J. and Al-Hashimi,H.M. (2007) Characterizing the relative orientation and dynamics of RNA A-form helices using NMR residual dipolar couplings. *Nat. Protoc.*, **2**, 1536–1546.
48. Zheng,G., Lu,X.J. and Olson,W.K. (2009) Web 3DNA–a web server for the analysis, reconstruction, and visualization of three-dimensional nucleic-acid structures. *Nucleic Acids Res.*, **37**, W240–W246.
49. Brooks,B.R., Brooks,C.L. III, Mackerell,A.D., Nilsson,L., Petrella,R.J., Roux,B., Won,Y., Archontis,G., Bartels,C., Boresch,S. *et al.* (2009) CHARMM: the biomolecular simulation program. *J. Comput. Chem.*, **30**, 1545–1614.
50. Feig,M., Karanicolas,J. and Brooks,C.L. III (2004) MMTSB Tool Set: enhanced sampling and multiscale modeling methods for applications in structural biology. *J. Mol. Graph Model.*, **22**, 377–395.
51. Lipari,G. and Szabo,A. (1982) Model-free approach to the interpretation of nuclear magnetic-resonance relaxation in macromolecules .2. Analysis of experimental results. *J. Am. Chem. Soc.*, **104**, 4559–4570.
52. Rieder,U., Kreutz,C. and Micura,R. (2010) Folding of a transcriptionally acting preQ1 riboswitch. *Proc. Natl Acad. Sci. USA*, **107**, 10804–10809.
53. Zuker,M. (2003) Mfold web server for nucleic acid folding and hybridization prediction. *Nucleic Acids Res.*, **31**, 3406–3415.
54. Adamiak,R.W., Blazewicz,J., Formanowicz,P., Gdaniec,Z., Kasprzak,M., Popenda,M. and Szachniuk,M. (2004) An algorithm for an automatic NOE pathways analysis of 2D NMR spectra of RNA duplexes. *J. Comput. Biol.*, **11**, 163–179.
55. Case,D.A. (1995) Calibration of ring-current effects in proteins and nucleic acids. *J. Biomol. NMR*, **6**, 341–346.
56. Cromsigt,J., Hilbers,C.W. and Wijmenga,S.S. (2001) Prediction of proton chemical shifts in RNA - Their use in structure refinement and validation. *J. Biomol. NMR*, **21**, 11–29.
57. Fares,C., Amata,I. and Carlomagno,T. (2007) 13C-detection in RNA bases: revealing structure-chemical shift relationships. *J. Am. Chem. Soc.*, **129**, 15814–15823.
58. Zhao,Y., Alipanahi,B., Li,S.C. and Li,M. (2010) Protein secondary structure prediction using NMR chemical shift data. *J. Bioinform. Comput. Biol.*, **8**, 867–884.
59. Kankia,B.I. (2003) Binding of Mg2+ to single-stranded polynucleotides: hydration and optical studies. *Biophys. Chem.*, **104**, 643–654.
60. Dethoff,E.A., Hansen,A.L., Musselman,C., Watt,E.D., Andricioaei,I. and Al-Hashimi,H.M. (2008) Characterizing complex dynamics in the transactivation response element apical loop and motional correlations with the bulge by NMR, molecular dynamics, and mutagenesis. *Biophys. J.*, **95**, 3906–3915.
61. Tolman,J.R., Flanagan,J.M., Kennedy,M.A. and Prestegard,J.H. (1997) NMR evidence for slow collective motions in cyanometmyoglobin. *Nat. Struct. Biol.*, **4**, 292–297.
62. Tjandra,N. and Bax,A. (1997) Direct measurement of distances and angles in biomolecules by NMR in a dilute liquid crystalline medium. *Science*, **278**, 1111–1114.
63. Tolman,J.R., Flanagan,J.M., Kennedy,M.A. and Prestegard,J.H. (1995) Nuclear magnetic dipole interactions in field-oriented proteins: information for structure determination in solution. *Proc. Natl Acad. Sci. USA*, **92**, 9279–9283.
64. Getz,M., Sun,X., Casiano-Negroni,A., Zhang,Q. and Al-Hashimi,H.M. (2007) NMR studies of RNA dynamics and structural plasticity using NMR residual dipolar couplings. *Biopolymers*, **86**, 384–402.
65. Tolman,J.R. and Ruan,K. (2006) NMR residual dipolar couplings as probes of biomolecular dynamics. *Chem. Rev.*, **106**, 1720–1736.
66. Getz,M.M., Andrews,A.J., Fierke,C.A. and Al-Hashimi,H.M. (2007) Structural plasticity and Mg2+ binding properties of RNase P P4 from combined analysis of NMR residual dipolar couplings and motionally decoupled spin relaxation. *RNA*, **13**, 251–266.
67. Sun,X., Zhang,Q. and Al-Hashimi,H.M. (2007) Resolving fast and slow motions in the internal loop containing stem-loop 1 of HIV-1 that are modulated by Mg2+ binding: role in the kissing-duplex structural transition. *Nucleic Acids Res.*, **35**, 1698–1713.
68. Zhang,Q., Stelzer,A.C., Fisher,C.K. and Al-Hashimi,H.M. (2007) Visualizing spatially correlated dynamics that directs RNA conformational transitions. *Nature*, **450**, 1263–1267.
69. Losonczi,J.A., Andrec,M., Fischer,M.W. and Prestegard,J.H. (1999) Order matrix analysis of residual dipolar couplings using singular value decomposition. *J. Magn. Reson.*, **138**, 334–342.
70. Musselman,C., Pitt,S.W., Gulati,K., Foster,L.L., Andricioaei,I. and Al-Hashimi,H.M. (2006) Impact of static and dynamic A-form heterogeneity on the determination of RNA global structural dynamics using NMR residual dipolar couplings. *J. Biomol. NMR*, **36**, 235–249.
71. Zweckstetter,M. (2008) NMR: prediction of molecular alignment from structure using the PALES software. *Nat. Protoc.*, **3**, 679–690.

Downloaded from http://nar.oxfordjournals.org/ at University of Michigan on February 14, 2012

72. Al-Hashimi,H.M., Majumdar,A., Gorin,A., Kettani,A., Skripkin,E. and Patel,D.J. (2001) Field- and phage-induced dipolar couplings in a homodimeric DNA quadruplex: relative orientation of G.(C-A) triad and G-tetrad motifs and direct determination of C2 symmetry axis orientation. *J. Am. Chem. Soc.*, **123**, 633–640.
73. Zhang,Q., Kang,M., Peterson,R.D. and Feigon,J. (2011) Comparison of Solution and Crystal Structures of PreQ(1) Riboswitch Reveals Calcium-Induced Changes in Conformation and Dynamics. *J. Am. Chem. Soc.*, **133**, 5190–5193.
74. Klein-Seetharaman,J., Oikawa,M., Grimshaw,S.B., Wirmer,J., Duchardt,E., Ueda,T., Imoto,T., Smith,L.J., Dobson,C.M. and Schwalbe,H. (2002) Long-range interactions within a nonnative protein. *Science*, **295**, 1719–1722.
75. Musselman,C., Zhang,Q., Al-Hashimi,H. and Andricioaei,I. (2010) Referencing strategy for the direct comparison of nuclear magnetic resonance and molecular dynamics motional parameters in RNA. *J. Phys. Chem. B*, **114**, 929–939.
76. Dethoff,E.A., Hansen,A.L., Zhang,Q. and Al-Hashimi,H.M. (2010) Variable helix elongation as a tool to modulate RNA alignment and motional couplings. *J. Magn. Reson.*, **202**, 117–121.
77. Zhang,Q. and Al-Hashimi,H.M. (2009) Domain-elongation NMR spectroscopy yields new insights into RNA dynamics and adaptive recognition. *RNA*, **15**, 1941–1948.

Downloaded from http://nar.oxfordjournals.org/ at University of Michigan on February 14, 2012